Alignment tolerances for off-plane reflection grating spectroscopy: theoretical calculations and laboratory techniques

Ryan Allured, Benjamin D. Donovan, Randall McEntaffer

Ryan Allured, Benjamin D. Donovan, Randall McEntaffer, "Alignment tolerances for off-plane reflection grating spectroscopy: theoretical calculations and laboratory techniques," Proc. SPIE 8861, Optics for EUV, X-Ray, and Gamma-Ray Astronomy VI, 88611C (26 September 2013); doi: 10.1117/12.2022873

Event: SPIE Optical Engineering + Applications, 2013, San Diego, California, United States

Alignment Tolerances for Off-Plane Reflection Grating Spectrometry: Theoretical Calculations and Laboratory Techniques

Ryan Allured[a], Benjamin D. Donovan[b], and Randall L. McEntaffer[b]

[a]Harvard-Smithsonian Center for Astrophysics, Cambridge, MA, USA;
[b]University of Iowa, Iowa City, IA, USA;

ABSTRACT

Off-plane reflection gratings can be used to provide high throughput and spectral resolution in the 0.3-2.0 keV band, allowing for unprecedented diagnostics of energetic astrophysical processes. A grating spectrometer consists of multiple aligned gratings intersecting the converging beam of a Wolter-I telescope. Each grating will be aligned such that the diffracted spectra overlap at the focal plane. Misalignments will degrade both spectral resolution and effective area. In this paper we present a summary of analytical alignment tolerance calculations, including an investigation of diffraction efficiency alignment dependence. Our plan for extending this work to future modeling and simulation is laid out. Finally, we report on the status of laboratory techniques to achieve these tolerances for flight-like optics.

1. INTRODUCTION

The development of critical technologies is required to accomplish the science goals of future NASA X-ray observatories. One such technology is off-plane reflection gratings to produce high throughput and high spectral resolving power at energies below 1.5 keV. Grating spectrometers are currently used onboard the *Chandra X-ray Observatory* and *XMM-Newton* as the main workhorses for X-ray spectroscopy with a resolution limit of 1000 ($\lambda/\delta\lambda$) and low effective area ($\lesssim 100$ cm^2) over the same band. Future goals of > 3000 spectral resolving power and effective areas of > 1000 cm^2 necessitate a new generation of high quality spectrometers capable of achieving these performance requirements.[9]

Off-plane reflection gratings are an attractive option for X-ray spectrometers. They offer compact packing geometries, excellent grating efficiency, and the potential for very high resolving powers. An array of off-plane gratings can be coupled with a set of nested Wolter-I optics (a primary parabolic mirror, followed by a secondary hyperbolic) to disperse a spectrum onto an imaging detector placed at the focal plane, typically a CCD camera.[7] The spectrum forms an arc of diffracted light in the shape of a cone, giving the common name for this type of diffraction—conical diffraction.

Fig. 1 depicts the grating geometry and outlines the necessary advancements. The image on the left is the canonical off-plane geometry with light intersecting a ruled grating nearly parallel to the groove direction. This creates an arc of diffraction at the focal plane with dispersion dictated by the displayed grating equation. The image on the right is similar, but has the optical axis pointing out of the page. The grating grooves are shown projected from the position of the gratings to a focal plane located several (typically ~ 8) meters away. High X-ray throughput requires high reflectivity and hence grazing incidence. To increase the total collecting area, many gratings are stacked into an array. Tight packing geometries are allowed because the cone angle of the diffracted light is roughly equal to the graze angle of the incoming light.

The effective area can be increased further by blazing the groove facets to a triangular profile that preferentially disperses light to one side of zero order. This requires a smaller readout detector (or less detectors in an array) and thus increases the signal-to-noise in these orders. The angle of the blaze on the grooves (θ in Fig. 1) is chosen to optimize diffraction efficiency toward the middle of the first order bandpass. This, in turn, translates to optimized efficiencies at higher orders for shorter wavelengths. The grating array is then rotated slightly about the grating normal resulting in an α for zero order at the focal plane that equals the β of the optimized wavelength. When $\alpha = \beta = \theta$ the array is in the Littrow configuration and is optimized for diffraction

Optics for EUV, X-Ray, and Gamma-Ray Astronomy VI, edited by Stephen L. O'Dell,
Giovanni Pareschi, Proc. of SPIE Vol. 8861, 88611C · © 2013 SPIE
CCC code: 0277-786X/13/$18 · doi: 10.1117/12.2022873

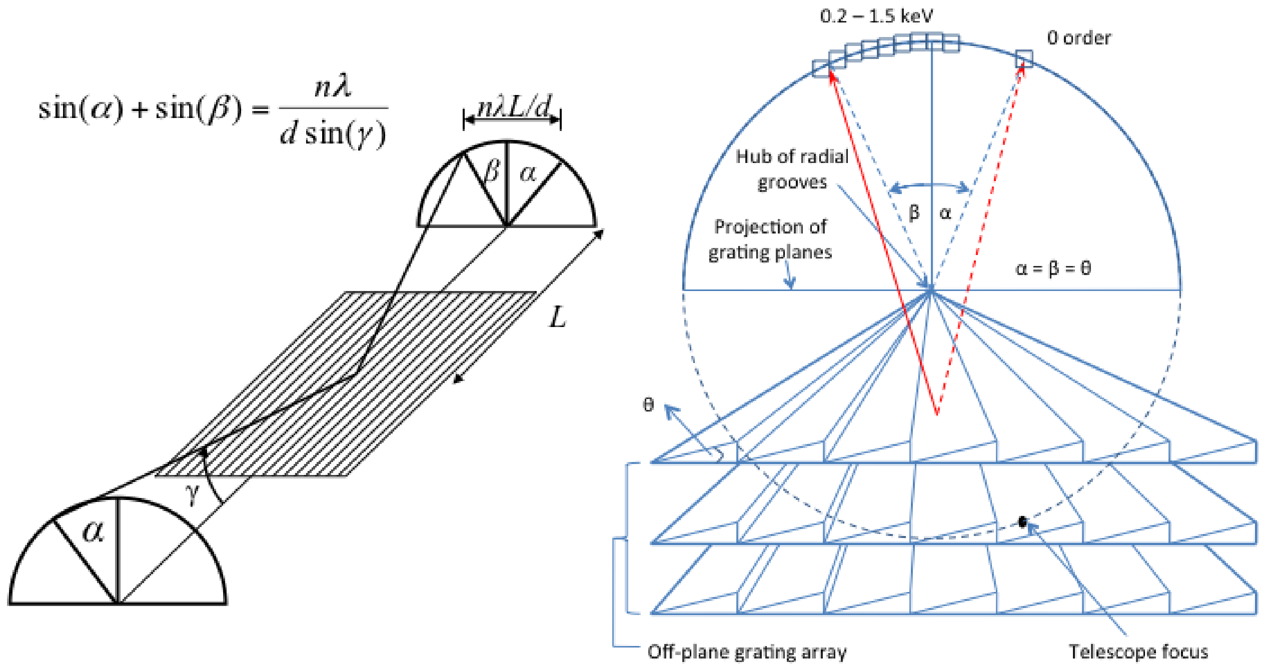

Figure 1. *Left* - The off-plane grating mount. *Right* - Three gratings, placed many meters from the focus, are shown projected onto the focal plane to elucidate the nature of the arc of diffraction which is detected by an array of CCDs (depicted as squares).

efficiency.[3] The similarity to the Littrow configuration in the in-plane diffraction sense can be seen by examining Fig. 1 and setting $\alpha = \beta$.

The projection of the grooves in Fig. 1 illustrates the radial distribution of grooves necessary to achieve high spectral resolving power.[3] This convergence matches that of the telescope beam, thus maintaining a constant α over the grating. This leads to a constant β per wavelength at the focal plane and eliminates grating induced aberration due to the groove profile. In other words, the converging rays from the Wolter I mirrors strike the grating at nearly the same angle with respect to the grooves at all points on the grating surface.

Fig. 1 also depicts the need for precision alignment within the off-plane grating array. The grooves on each grating converge to a point at the center of the circle defined by the intersection of the cone of diffraction with the focal plane. This focal circle is also coincident with the telescope focus and the zero order focus. The gratings within an array are aligned such that all groove hubs are coincident. Also, all grating surfaces must project to the diameter of the focal circle. With these alignments achieved, the spectra from each grating overlap at the focal plane.

This paper reports on the status of the off-plane grating alignment program based at the University of Iowa. We summarize theoretical calculations producing analytical alignment tolerances and the raytracing used to verify them. Then, a plan is laid out for future simulation work that will lead to convergence to a flight-like spectrometer design. In the laboratory, significant progress has been made in controlling and measuring optic alignment to the precision of our analytical tolerances. Our system for optic actuation, alignment measurement, and figure measurement is outlined and the current performance summarized.

2. ANALYTICAL CALCULATIONS

This section summarizes analytical calculations producing alignment tolerances for all six degrees of freedom. For a more detailed report, please see Ref. 1, from which much of this text was taken.

2.1 Mathematical Formalism

Harvey & Vernold (1998) describe a convenient formalism for predicting the diffraction of light incident upon a parallel groove reflection grating for arbitrary grating orientation with respect to the incident beam. This formalism makes use of direction cosines for the incident and diffracted rays, and the coordinate system used in this paper is shown in Fig. 2. α_i and β_i are the direction cosines of the incident beam, α_0 and β_0 are the direction cosines of the undiffracted, specularly reflected beam, and α_m and β_m are the direction cosines of the diffracted beam of the mth order. In the figure, the grating grooves are aligned with the $\hat{\beta}$ axis. The angle between the grating grooves and the $\hat{\alpha}$ axis is given by Ψ. In Fig. 2, $\Psi = 90°$ and the grooves are aligned with the $\hat{\beta}$ axis. This formalism is completely general and reduces to that of Fig. 1 in the limit of $\Psi \to 90°$. Note that these coordinates are not related to the angles α and β in Fig. 1.

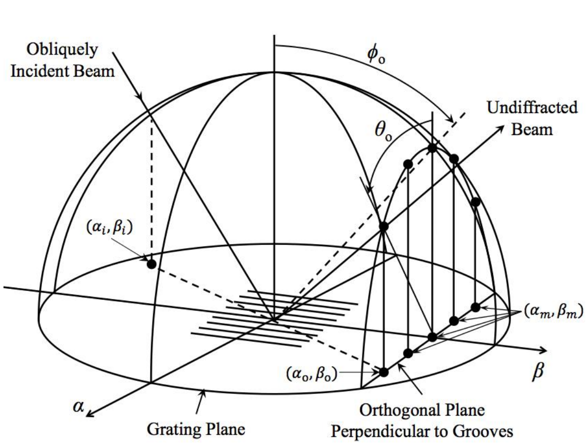

Figure 2. The mathematical description of the off-plane grating geometry. α_i, β_i describe the orientation of the incident beam, α_0, β_0 describe the orientation of the specularly reflected beam, and α_m, β_m describe the orientation of the various orders of diffraction. Adapted from Harvey & Vernold (1998).

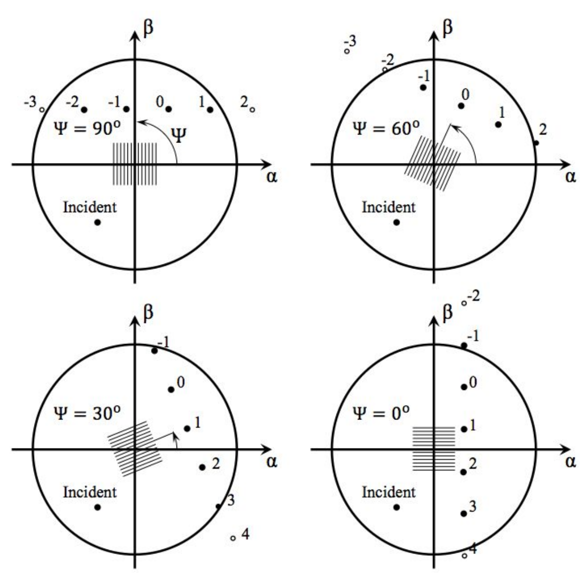

Figure 3. Direction cosine diagrams for diffraction with various yaw angles Ψ. The location of zero order is set by the specular reflection of the incident beam. As Ψ changes, the line of diffraction in cosine space rotates about zero order. In this framework, the transition from classical in-plane diffraction to conical off-plane diffraction can be easily understood. Adapted from Harvey & Vernold (1998).

Using these coordinates, the equations giving the diffracted directions for arbitrary beam incidence and grating orientation are

$$\begin{aligned} \alpha_m + \alpha_i &= (m\lambda/d)\sin\Psi \\ \beta_m + \beta_i &= -(m\lambda/d)\cos\Psi \end{aligned} , \tag{1}$$

where $\alpha_m = \sin\theta_m \cos\phi_m$, $\beta_m = \sin\phi_m$, $\alpha_i = -\sin\theta_0 \cos\phi_0$, and $\beta_i = -\sin\phi_0$. Fig. 3 shows the various diffracted orders in direction cosine space for various grating orientations. The zero order, specularly reflected beam location is fixed based on the incident beam's location, the spacing of the various orders is dictated by the wavelength λ and groove period d, and the orientation of the line of diffraction in direction cosine space is dictated by the grating orientation Ψ. Orders lying outside the $\alpha^2 + \beta^2 = 1$ circle in direction cosine space are so-called evanescent orders, and are not observed in real space.

2.2 Assumptions

For our initial grating alignment calculations, we use radial gratings with a groove period of $d = 160$ nm at an 8 m distance from the hub. Longer wavelength light is diffracted at larger angles, requiring tighter alignment tolerances. Thus, we assume a wavelength of 4.1 nm, corresponding to an energy of 0.3 keV (the low end of our desired energy range). We take a characteristic initial beam alignment with an incidence angle $i = 88.5°$ and $\theta_0 = -18°$, where $\sin i = \cos\phi_0 \cos\theta_0$. This θ_0 will optimize the grating for a first order Littrow configuration at a wavelength of roughly 4 nm. The sign of θ_0 is arbitrary; one of the first order beams is diffracted into evanescence, while the other is available for spectroscopy. We set our nominal yaw to $\Psi = 90°$. Finally, we assume a flat focal plane positioned a distance $L = 8$ m from the nominal beam impact point (the origin in Fig. 2) along the $\hat{z}$ axis and parallel to the xy plane. This distance is typical of X-ray grating spectrometer architectures recently studied by NASA.[2,8]

2.3 Spot Shift Requirements

Reflection grating spectroscopy turns the spectral resolution problem into a spatial resolution problem. Photons will be dispersed in the $\hat{x}$ direction based on their wavelength. Thus, we map a photon's x position on the detector to wavelength or energy regardless of its y position as evident in the upper left panel of Fig. 3. For a single grating, the spectral resolution is then dictated by the point spread function of the diffracted image in the $\hat{x}$ direction. With current sub-apertured Wolter I optics produced by Zhang et al. (2012), the line spread function (LSF) in the dispersion direction ($\hat{x}$) is approximated by a line with a 1 arcsecond full width at half maximum (FWHM). The line width is oriented in the dispersion direction so that energy resolution is dictated by the 1 arcsecond spread. For our throw length (L), this is equivalent to roughly 40 μm. Thus, an estimate of our spectral bin size is 40 μm.

When a second grating is integrated into the spectrometer array, it must be aligned such that its arc of diffraction coincides with that of the first grating. Misalignments, both angular and translational, will cause the diffracted beam of a given order and wavelength to shift. Our initial goal is to limit this shift in the $\hat{x}$ direction to less than 40 μm (the spectral bin size) at the detector plane. As a first step, we will calculate the maximum allowable misalignment for each independent degree of freedom. The 40 μm spot shift limit is somewhat arbitrary; the actual spot shift requirement for an instrument would flow down from a top level spectral resolution requirement. This will be addressed in a future paper investigating both coupled alignment tolerances and optimization of spectral resolution and diffraction efficiency. Misalignments in the orthogonal direction ($\hat{y}$) will reduce sensitivity by spreading the diffraction arc over a larger detector area. We choose a similarly arbitrary $\hat{y}$ spot shift limit of 378 μm based on the 10 arcsecond point spread function (PSF) of the full telescope.

To calculate the effect a given misalignment has on a photon's x position at the focal plane, we must express x as a function of α_m and β_m. Let Θ be the angle between the $\hat{z}$ (or $\hat{\beta}$) axis and the projection of the diffracted beam onto the xz plane. The distance between the beam impact point and the focal plane is L, thus the beam's x position at the focal plane is $L\tan\Theta$. Θ can also be expressed as $\arctan(\alpha_m/\beta_m)$, leading to $x = L\alpha_m/\beta_m$. Finally, to calculate the shift in x position of the mth diffracted beam due to a misalignment, initial (subscript 0) and final (subscript 1) direction cosines can be used to obtain

$$\Delta x = L_1(\alpha_{m,1}/\beta_{m,1}) - L_0(\alpha_{m,0}/\beta_{m,0}), \tag{2}$$

where $L_0 = 8$ m and L_1 is the final throw length after a possible shift in the beam impact location due to translations of the grating. Similarly, the photon's $\hat{y}$ displacement can be expressed as

$$\Delta y = L_1 \tan(\arcsin(\gamma_{m,1})) - L_0 \tan(\arcsin(\gamma_{m,0})), \tag{3}$$

where γ is the direction cosine in the $\hat{\alpha} \times \hat{\beta}$ direction. The third direction cosine can easily be calculated using $\gamma = \sqrt{1 - \alpha^2 - \beta^2}$.

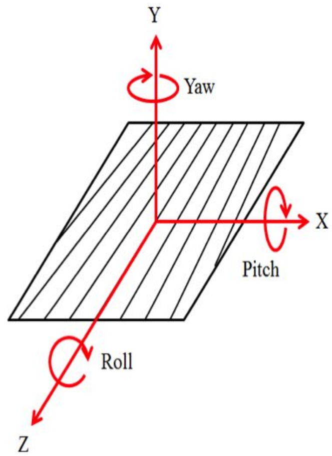

Figure 4. Definition of the degrees of freedom given in Table 1.

2.4 Results

The above equations were used to calculate the misalignments at which the spot shift requirements were violated. These tolerances are reported in Table 1 along with the requirement (spectral resolution or effective area) violated by the misalignments. Raytracing a flight-like spectrometer with Wolter I optics and the same geometric assumptions was used to verify these tolerances. Both analyses produced identical tolerances. Note that these are absolute, not statistical, alignment tolerances. They also assume perfect alignment for the other five degrees of freedom. The six degrees of freedom are defined in Fig. 4.

Table 1: Analytical Alignment Tolerance Summary

Misalignment	Tolerance	Limiting Effect
Yaw	± 7.9 arcsec	Effective Area
Pitch	± 4.3 arcsec	Effective Area
Roll	± 21.6 arcsec	Spectral Resolution
$\hat{x}$	± 317 μm	Effective Area
$\hat{y}$	± 170 μm	Effective Area
$\hat{z}$	± 1.51 mm	Spectral Resolution

2.5 Diffraction Efficiency Calculations

If the diffraction efficiency per grating were to change appreciably due to misalignments, calculating the effective area of the grating spectrometer would have to take this into account. In fact, this would also greatly complicate the energy response function of the spectrometer: the precise alignment of each mirror pair and grating would need to be known to compute the on-axis energy response function, and an off-axis source could potentially change the response function in a significant manner. Fortunately, we have performed efficiency simulations that show this is not a concern for our expected misalignments.

We use the commercial software PCGrate-S(X) v.6.1 © (I.I.G. Inc.) to compute our efficiencies, as the dependence of diffraction efficiency on beam geometry and wavelength is a complicated computational problem (see Neviere & Popov 1998 for a review). The software works by solving a system of integral equations over the periodic groove boundary. We assume a grating with an 18° blaze angle and a 160 nm period. The groove profile is right triangular, and the groove material is gold. The nominal θ_0 and ϕ_0 are as in §2.2. The normal computation mode is used with the standard options, and we obtain normal accuracy conditions (e.g. relative efficiency summed over all orders is 1) for all calculations reported in this paper.

After an angular or translational misalignment, three parameters relating to diffraction efficiency can change: θ_0, ϕ_0, and groove period d. Characteristic limits on these parameters are ± 22 arcseconds, ± 4 arcseconds,

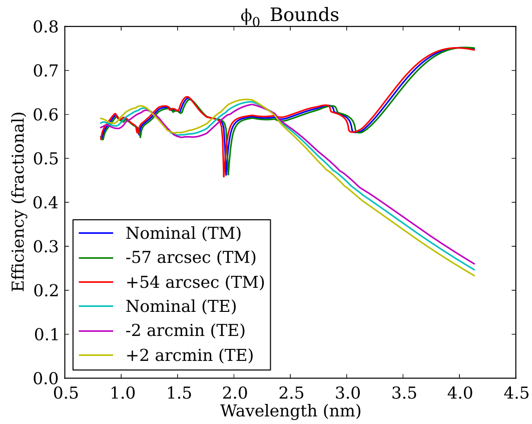

Figure 5. Diffraction efficiencies for both transverse electric (TE) and transverse magnetic (TM) polarizations for a nominal (88.4228°) and misaligned ϕ_0. For our angular misalignment tolerances, the maximum change in ϕ_0 is ± 4 arcseconds (pitch).

and ± 0.03 nm, obtained from the roll, pitch, and $\hat{z}$ translation tolerances above. Our goal was to determine bounds on these parameters based on when the diffraction efficiency changes appreciably. An appreciable change was defined as a $> 1\%$ RMS difference in diffraction efficiency over the 300–1500 eV (4.1–0.8 nm) range. For each parameter of interest, the value was shifted away from the nominal value in an iterative process until this change condition was reached. This was done for both transverse electric (TE) and transverse magnetic (TM) polarizations. Figs. 5 shows the nominal diffraction efficiency and the diffraction efficiency after the change condition was reached in both the positive and negative direction for ϕ_0. Note that the dramatic dependence on polarization is an expected result, and such a dependence has been measured in the past.[11] In all cases, the misalignments which result in the 1% RMS efficiency change are at least an order of magnitude greater than the characteristic limits given above. They are also much greater than the pointing stability of a typical X-ray observatory (~ 0.25 arcseconds for *Chandra*). These results indicate that a single diffraction efficiency curve can be used to determine effective area, and that the effective area (i.e. energy response function) can be assumed to be constant during a telescope pointing.

3. FUTURE MODELING WORK

Our modeling work has thus far been restricted to analytical tolerance verification and efficiency alignment dependence. This section outlines our plan for simulations that will produce a statistical alignment budget and a flight-like spectrometer design.

3.1 Grating Placement and Focal Plane Optimization

In a flight-like spectrometer design, gratings are matched to a set of focusing optics. This can most easily be envisioned as a fanned array redirecting the output of conventional Wolter I optics as in Fig. 6. Other geometries are possible such as that for the OGRE rocket payload being developed at the University of Iowa.[5] Regardless of the specific design, an array of gratings will be used to create overlapping diffraction arcs in the focal plane. However, conical diffraction occurs in the off-plane analog of the Rowland circle as in Fig. 7. For a given ray, the origin of this circle lies at its intercept with the grating. Therefore, the origins of the diffraction circles in an off-plane reflection grating array will not coincide. This will result in aberrations at the focal plane.

To minimize these aberrations, the nominal focal plane may be curved. This is achieved in practice by adjusting the positions of CCDs in the focal plane array. The size of the individual CCDs dictates how precisely the ideal focal plane curvature may be followed. A larger number of smaller sized CCDs will be more effective at reducing aberrations, but will also add complexity to the instrument. The relationship of CCD size on field curvature aberration reduction will be investigated using our existing raytrace.

Furthermore, the precise way in which the gratings are aligned to one another will be investigated to determine the optimum configuration for aberration reduction. To date, most authors have proposed aligning the grating hubs to one another.[4,7] Other approaches, such as aligning the zero order foci or even the theoretical first order foci for a given wavelength are certainly feasible. A variety of grating placement schemes will be raytraced to determine which results in the lowest aberration over our bandpass of interest.

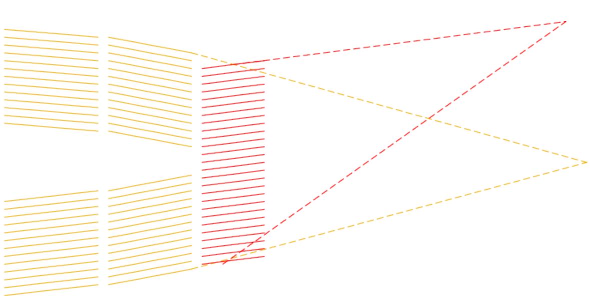

Figure 6. A conceptual diagram of a grating array placed in the path of a converging Wolter I telescope. Each grating must be aligned to a particular Wolter I shell in order to produce coincident diffraction patterns at the focal plane. In other words, the array of gratings is fanned in order to match the cone angles of the Wolter I mirrors.

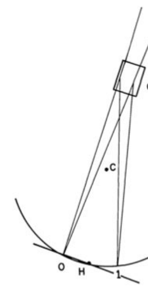

Figure 7. A conceptual diagram of the off-plane analog of the Rowland circle. The conical diffraction pattern from a given ray forms a focal sphere, the center of which is at the nominal ray intercept with the grating. From Cash (1983).

3.2 Monte-Carlo Error Budget

The analytical tolerances given in Table 1 are isolated in that they assume perfect alignment for all but one degree of freedom. An actual error budget must come from a Monte-Carlo raytrace. This will be accomplished by adding random Gaussian misalignments to all six degrees of freedom in our raytrace and measuring the resultant photon distribution in both the spectral direction and the orthogonal direction. The magnitudes of the misalignments will be reduced until the distribution widths meet our spectral resolution and effective area requirements. Furthermore, the allocation of errors among the six degrees of freedom will be tweaked to tighten relatively loose tolerances in order to loosen relatively tight tolerances.

3.3 Figure of Merit Optimization

For given spectral resolution and diffraction efficiency requirements, there will be a finite range of useful wavelengths for a given diffraction order. The lower bound on this range is typically dictated by the point at which $\lambda/\delta\lambda$ drops below the required resolution. The upper bound is typically dictated by the wavelength at which the diffraction efficiency falls below the requirement. This is not a steadfast rule, as the diffraction efficiency requirement may be violated before the spectral resolution requirement as the wavelength decreases, depending mostly on the grating blaze angle. Fig. 8 shows an early raytrace of diffraction arcs of various orders separated by an arbitrary displacement in the $\hat{y}$ direction. Only the useful ranges of each diffraction order are plotted.

The total spectrometer effective area is then based on the sum of diffraction efficiency over all useful orders. The bounds of this summation essentially depend on three things: the effective PSF based on the misalignment error budget, the spectral resolution and effective area requirements, and the diffraction efficiency of the gratings. The effective PSF is tunable by relaxing or tightening alignment requirements, and the diffraction efficiency is tunable by adjusting the blaze angle within realistic limits (roughly $0-20$ degrees). The interplay between these spectrometer attributes will be fully explored in our raytrace. This will culminate in a program for optimization of a figure of merit defined as spectral resolution times diffraction efficiency.

4. LABORATORY ALIGNMENT

In addition to solidifying our understanding of grating spectrometer alignment requirements, we have developed a laboratory alignment and metrology system capable of meeting our preliminary tolerances. This section first

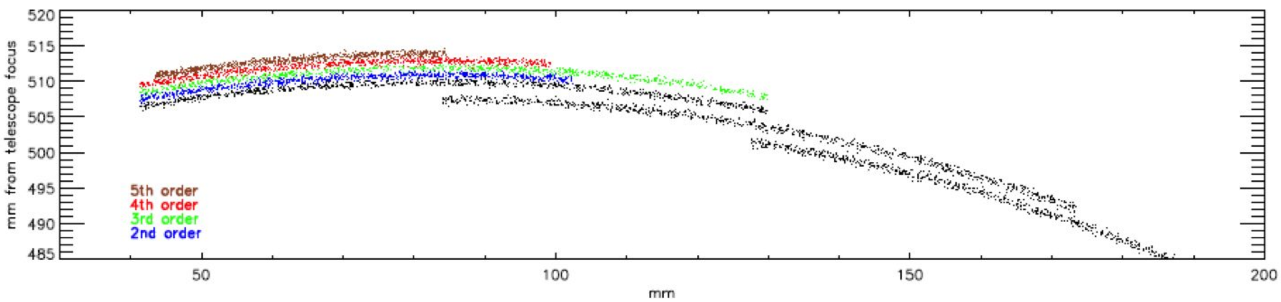

Figure 8. An early raytrace of various diffraction orders from a flight-like spectrometer. The three black arcs are continuous spectra from three misaligned optics modules. The colored arcs are diffraction orders exploded out from the topmost spectrum. There is an arbitrary $\hat{y}$ displacement added to the orders to separate them visually. Only the spectrally useful range of each order has been plotted. This range is limited both by diffraction efficiency and spectral resolution.

describes our current system for aligning test plates of flight-like grating dimensions. Metrology systems featuring a Shack-Hartmann wavefront sensor for alignment and figure measurement are then detailed. We summarize with future plans for laboratory alignment of gratings.

4.1 Mount and Actuation Mechanism

A medium fidelity mount and actuation mechanism was fabricated by the University of Iowa machine shop in early 2013 and is shown in Fig. 9. It can be used to align test plates of the same 100×100 mm^2 footprint and 0.4 mm thickness as planned for flight gratings. Newport 8310 Picomotors provide alignment in five degrees of freedom. Their nominal step size of 30 nm produces ~ 0.1 arcsecond angular steps of the test plates. The remaining degree of freedom is $\hat{z}$ translation and is mechanically constrained by a guard rail. The initial position of a test plate is constrained by precision bosses and compression springs shown in Fig. 10. A reference plate is slid into the first set of bosses, constrained with springs, and bonded into place. Subsequent plates are installed with springs pressing against the previous plate. The alignment of each plate is adjusted in reference to the previous plate prior to bonding. The test plates currently being tested are composed of nickel coated beryllium. This fixture, or something closely resembling it, will eventually be used to align two radially grooved gratings (fabricated using Si wafers) for X-ray testing with Wolter I optics.

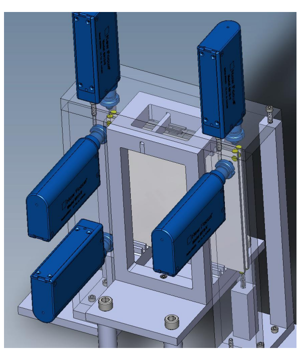

Figure 9. A CAD drawing of the medium fidelity mount and actuation fixture machined at the University of Iowa. Newport 8310 Picomotors provide ~ 0.1 arcsecond angular control.

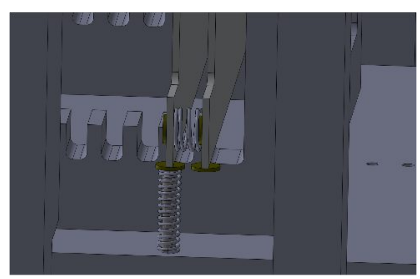

Figure 10. A close up of the springs used to constrain the initial position of the test plates (or gratings). The yellow circles represent sapphire pads used for contact with the Newport actuators.

4.2 Alignment Measurement

Our alignment metrology system is shown in Fig. 11. A gimbal mounted laser diode reflects off of the test plate and is monitored by a Thorlabs WFS150-7AR Shack-Hartmann sensor. As the orientation of the test plate is adjusted, the WFS detects changes in the tilt of the reflected beam. For alignment of one test plate to another, the laser diode and WFS must not be disturbed between plate measurements. The alignment fixture must also be stable against the forces seen during the installation of plates. To test this, the orientation of a test plate was monitored for roughly 10 days with occasional mechanical nudging. The data is shown in Fig. 12, where the vertical dashed lines indicate either both the plate and the fixture were nudged or just the plate was nudged. The system is stable to < 1 arcsecond per hour of drift and less than 2 arcseconds shift after nudging.

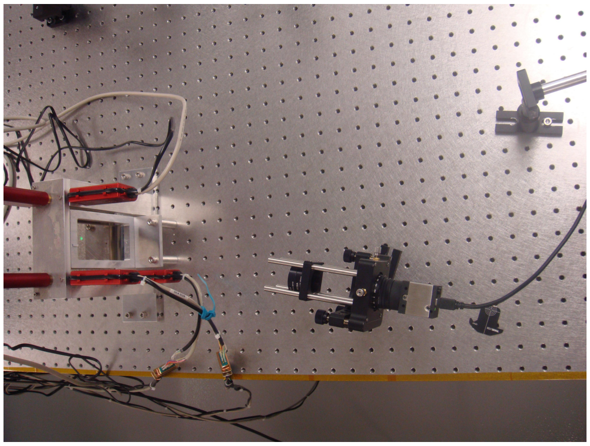

Figure 11. A photo of our alignment metrology system. The reflection of the laser diode (upper right) from the alignment test plate (left) is monitored by a Thorlabs Shack-Hartmann wavefront sensor (lower right).

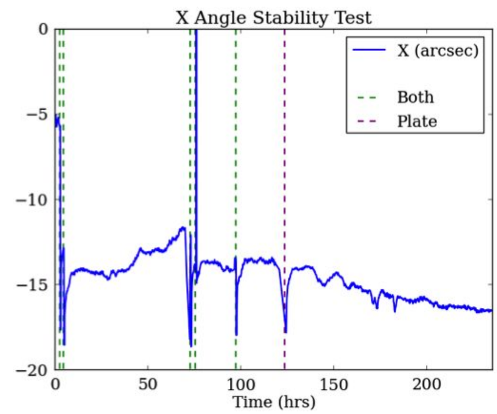

Figure 12. One of two orthogonal angles of the reflected laser beam during an alignment system stability test. The vertical dashed lines indicate either both the alignment fixture and test plate were nudged or just the test plate was nudged. The system is stable to < 1 arcsecond per hour of drift and less than 2 arcseconds of shift after nudging.

Angular step size, hysteresis, and degree of freedom mixing were investigated using the data in Figs. 13 and 14. The pitch and roll angle of a test plate were monitored while either the pitch or roll actuator was stepped forward and then backwards in 3 steps of 10 actuation steps. The achieved angular steps were ~ 2.5 arcseconds. This implies a ~ 0.125 arcsecond control of the plates, accounting for the factor of 2 difference between reflected beam alignment and plate alignment. A small amount of hysteresis is present in each test, but is non-problematic for an alignment convergence algorithm. Also present is a small amount of degree of freedom mixing, particularly in the pitch test (Fig. 13). However, this is also believed to be non-problematic in an alignment convergence algorithm.

4.3 Figure Measurement

The process of mounting and bonding thin gratings or mirrors is known to induce deformations known as figure error. In order to verify that our alignment techniques do not introduce unacceptable figure error to our gratings, we require a metrology system to measure the 2D surface profile of mounted gratings. To accomplish this, we introduce a Keplerian beam expander to illuminate the grating surface with a ~ 2 inch laser beam. For cost concerns, we have chosen to scan the WFS over the reflected expanded beam as opposed to purchasing a high-precision beam reducer. Individual WFS images are then stitched together to reconstruct the entire reflected wavefront. Grating surface errors will be imprinted into this wavefront. The general concept is shown in Fig. 15.

Our WFS has been mounted and aligned to a set of linear translation stages to enable wavefront stitching. Spherical lenses have been installed to expand our laser diode from ~ 5 mm to ~ 50 mm in diameter, and the expanded beam has been aligned to our staged WFS. We are currently perfecting our wavefront stitching algorithm, and the goal is to produce stitched contour plots similar to the WFS image of a standard Si wafer shown in Fig. 16. This data may then be analyzed to quantify mounting induced figure error. Our spatial wavelength sensitivity is limited by the 150 μm pixel size and the diameter of the expanded beam.

The Keplerian beam expander has been adjusted to produce a slightly diverging wavefront to test the stitching process. Fig. 17 shows 1D slices of the resultant stitched wavefront. We are able to measure very fine curvature

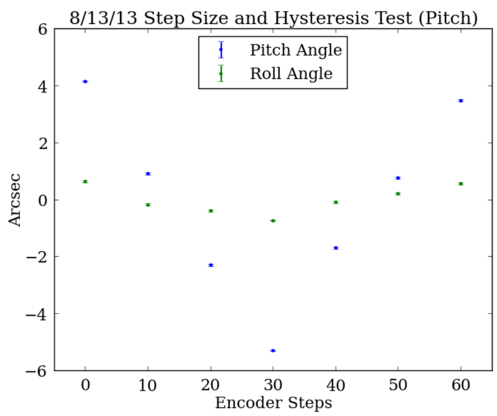

Figure 13. The pitch angle and roll angle of the reflected beam after adjustment of the pitch actuator. The ~ 2.5 arcsecond shifts of the reflected beam after 10 actuation steps indicate roughly 0.1 arcsecond control of the test plate.

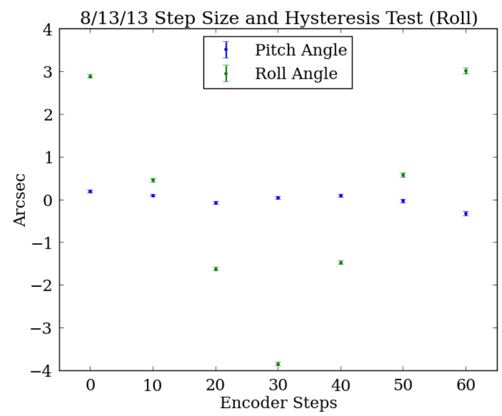

Figure 14. Same as Fig. 13, but instead the roll actuator was adjusted.

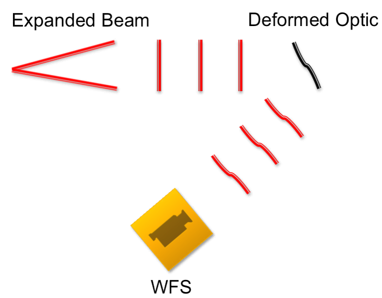

Figure 15. The conceptual diagram of our figure measurement system. A laser diode is expanded to a 2 inch diameter. The reflection of the beam off of the optic leaves surface deformations imprinted in the wavefront. A Shack-Hartmann wavefront sensor is scanned over the reflected beam to reconstruct the figure of the optic.

on top of a ~ 50 nm noise ripple. This noise is periodic due to WFS calibration issues, however, and may be removable from the data. All that remains is to perfect the algorithm that matches WFS image edges to produce large format wavefront measurements.

4.4 Future Work

Our mounting and alignment fixture and metrology system is currently operating within the alignment tolerances given in §2.4. Nevertheless, we believe we will be able to greatly improve the system stability, particularly the stability to alignment forces or nudging. After a best effort to improve system stability, we will demonstrate proper relative alignment of a pair of flight-like Si wafers. Once a pair of large format, radially grooved gratings is fabricated, the system will be used to align them for X-ray testing with a pair of Wolter I optics provided by Goddard Space Flight Center.[12]

Only a few minor issues remain with our figure error metrology system. Once the WFS image stitching algorithm is perfected, we will immediately proceed to measuring mounting induced figure error of large format Si wafers. If these figure errors are determined to be unacceptable, we will be able to experiment with different mounting and bonding techniques to reduce them. Measurement of the figure of a Si wafer before and after mounting will be our means of quantifying our success.

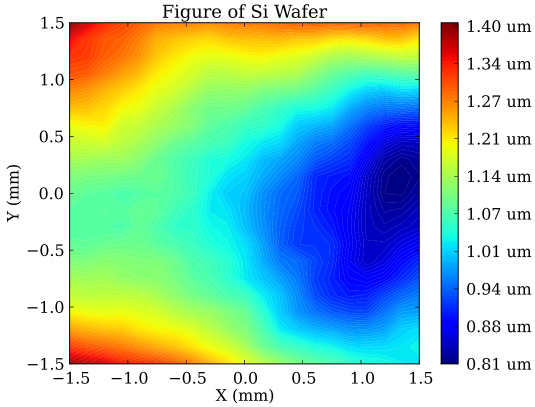

Figure 16. A single WFS image of a standard Si wafer. The 3 mm by 3 mm camera size is the standard for this model. An arbitrary 1 μm has been added to the pixel values to improve plot readability.

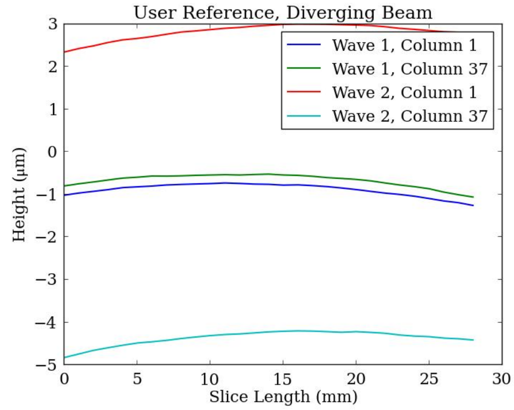

Figure 17. 1D slices of a stitched wavefront of a weakly diverging beam. Each curve represents a slice taken at a different position. There is a $\sim$ 50 nm periodic noise ripple in the data due to WFS calibration error.

5. SUMMARY

We have analyzed grating alignment tolerances using reasonable assumptions. This has given us a strong understanding of the required precision in mounting and aligning an array of gratings for a flight-like spectrometer. Future modeling will investigate optimal grating and focal plane placement, produce a statistical grating alignment error budget, and optimize a grating spectrometer figure of merit. Substantial progress has been made in the lab toward mounting and aligning test plates to the analytical tolerances. Furthermore, a figure measurement metrology system has been nearly perfected. The very near future will involve the completion of our laboratory alignment systems, and in the next year we will demonstrate alignment of flight-like, radially grooved gratings.

ACKNOWLEDGMENTS

The authors acknowledge support from NASA Strategic Astrophysics Technology grant, NNX12AF23G. The commercial software PCGrate-S(X) v.6.1 © (I.I.G. Inc.) was also crucial in the completion of this work.

REFERENCES

1. Allured, R., & McEntaffer, R. L. 2013, Analytical alignment tolerances for off-plane reflection grating spectroscopy, Accepted by Experimental Astronomy, arXiv:1308.5370
2. Bautz, M. W., et al., Concepts for high-performance soft X-ray grating spectroscopy in a moderate-scale mission, Proc. SPIE, 8443, 15-23 (2012)
3. Cash, W. C., Jr. 1983, Applied Optics, 22, 3971
4. Cash, W., X-ray optics: a technique for high resolution imaging, Applied Optics, 26, 2915-2920 (1987)
5. DeRoo, C., McEntaffer, R. L., Shultz, T., Zhang, W. W., Murray, N. J., O'Dell, S. L., & Cash, W. C., Jr. Pushing the boundaries of X-ray grating spectroscopy in a suborbital rocket, Proc. SPIE, 8861.
6. Harvey, J.E. and Vernold, C.L. Applied Optics, Vol. 37, Issue 34, pp. 8158-8160 (1998)
7. McEntaffer, R. L., et al., Developments of the off-plane x-ray grating spectrometer for IXO, Proc. SPIE, 7732, 48-60 (2010)
8. McEntaffer, R. L., Cash, W., Lillie, C., Casement, S., Zhang, W., Holland, A., Murray, N., O'Dell, S., Schattenburg, M., Heilmann, R., & Tsunemi, H., Development of off-plane gratings for WHIMex and IXO, Proceedings of the SPIE, 8147, 81471K-81471K-11 (2011)
9. McEntaffer, R., DeRoo, C., Schultz, T., et al. 2013, Experimental Astronomy, 36, 389
10. Neviere, M., & Popov, E. K. 1998, SPIE Proc., 3450, 2

11. Seely, J.F., Goray, L.I., Kjornrattanawanich, B., Laming, J.M., Holland, G.E., Flanagan, K.A., Heilmann, R.K., Chang, C.H., Schattenburg, M.L., and Rasmussen, A.P., Efficiency of a grazing-incidence off-plane grating in the soft X-ray region, Applied Optics, 45, 8 (2006)
12. Zhang, W. W., Biskach, M. P., Blake, P. N., et al. 2012, SPIE Proc., 8443